



Comparative study of arterial wall models for numerical fluid–structure interaction simulation of aortic arch aneurysms

Mário Luis Ferreira da Silva¹ · Saulo de Freitas Gonçalves¹ · Rudolf Huebner²

Received: 14 October 2021 / Accepted: 19 March 2022 / Published online: 7 April 2022
© The Author(s), under exclusive licence to The Brazilian Society of Mechanical Sciences and Engineering 2022

Abstract

The arterial wall model adopted in the fluid-structural numerical simulations is directly related to its mechanical response, as well as to the flow field. The work developed here compares different arterial wall models for an aneurysm located in the aortic arch. Isotropic linear elastic, Yeoh isotropic polynomial hyperelastic, and Holzapfel anisotropic hyperelastic models were used. Physiological boundary conditions were used throughout the cardiac cycle, and the non-Newtonian model of Carreau was used as rheological model. The fluid domain was discretized by the finite volume method, and the solid domain was discretized by the finite element method. The results showed that the less stiff model, i.e., the isotropic linear elastic model with modulus of elasticity $E = 1$ MPa, had a greater increase in the aneurysmal sac, which favored recirculation and induced low values of wall shear stress, which may be an indication of intraluminal thrombus formation overestimation. However, the peak of maximum principal stress, which occurred at the junction of supra-aortic branches with aortic arch, was higher in the Yeoh model, which may represent an overestimation of the rupture risk in stiffer models.

Keywords Aortic wall model · Fluid–structure interaction · Aortic arch aneurysm · Pulsatile blood flow · Hemodynamics

1 Introduction

Aortic arch aneurysms account for approximately 21.3% of cases of thoracic aortic aneurysms (TAA) [1]. Due to its anatomical characteristics, repair of aortic arch aneurysms by conventional or hybrid surgery remains a challenge, as these procedures are associated with high morbidity and mortality [2, 3]. In this context, computational numerical simulations of fluid–structure interaction (FSI) have become an important technique in the pathophysiology of the aneurysm and the development of new clinical devices.

The aortic artery wall is composed of a complex three-dimensional structural organization of elastin, collagen,

and smooth muscle cells [4]. The microstructure of the wall strongly influences its mechanical response, so histological evidence suggests that it has a non-linear behavior [4–9]. Furthermore, the arterial wall has anisotropic behavior, with greater stiffness in the circumferential direction, mainly due to collagen dispersion [6, 7, 10]. While some studies have reported an increase in anisotropy during aneurysm progression, due to changes in structural wall components [10–12], others indicated an increase in isotropy [6, 13]. Niestrawska et al. [14] argued that in the first stage of the aneurysm, the response is anisotropic due to collagen realignment in the circumferential direction, but in advanced stages, new collagen is isotropically deposited.

Stiffer aneurysm walls have been related to higher peak wall stress (PWS) and a higher risk of rupture [15]. On the other hand, less stiff aneurysms have been related to a shorter rupture time [16]. Low PWS may be associated with ILT formation and reduced wall strength [17]. In a direct comparison, isotropic hyperelastic models had higher PWS than the isotropic linear elastic model [18, 19]. Schmidt, Pandya and Balzani [20] discussed the influence of anisotropy on numerical arterial models in idealized geometries, showing that in the anisotropic model the deformations were smaller than in the

Technical Editor: Daniel Onofre de Almeida Cruz.

✉ Mário Luis Ferreira da Silva
marioluisfs@gmail.com

¹ Graduate Program in Mechanical Engineering, Department of Mechanical Engineering, Universidade Federal de Minas Gerais, Antônio Carlos Avenue, Pampulha, 6627, Belo Horizonte, MG 31270-901, Brazil

² Department of Mechanical Engineering, Universidade Federal de Minas Gerais, Antônio Carlos Avenue, Pampulha, 6627, Belo Horizonte, MG 31270-901, Brazil

isotropic one, unlike de Gelidi and Bucchi [21], where the deformations in the anisotropic model were greater. Lin et al. [22] compared an isotropic hyperelastic model with Holzapfel anisotropic hyperelastic model for a concentric saccular aneurysm of the abdominal aorta in which the results show that there was a movement on the anterior side of the aneurysm due to anisotropic orientation of the fibers, which, therefore, was not properly captured in the isotropic model.

The aortic arterial wall model also influences the blood flow field [18]. Stiffer aneurysm walls seem to overestimate wall shear stress (WSS) [22, 23] and inhibit vortex dissipation [22]. Unphysiological values of WSS can trigger diseases such as aneurysm, atherosclerosis, wall remodeling, and intraluminal thrombus (ILT) formation [23–27], however, the real effect of WSS on aneurysmal tissue damage is still open [28]. Low WSS values have been linked to the process of ILT formation [25–27], which favors wall weakening and aneurysm growth [29]. On the other hand, high WSS has been linked to reduced abundance of elastin and smooth muscle cells, which can lead to wall degradation [23].

Some studies adopted a statically determinate approach to the thoracic aorta wall [30, 31], however, unlike the abdominal aorta, the thoracic aorta presents wall stress dependent on the constitutive model, material properties, and geometry [32]. Although several anisotropic models were proposed for numerical simulation considering the complex microstructure of the aortic arterial wall [8, 9, 33, 34], isotropic linear elastic models and isotropic hyperelastic models have been used in the modeling of the aortic wall, probably due to their simple implementation. At the same time, specific studies of FSI numerical simulations for aortic arch aneurysms are scarce in the literature. Thus, the work proposed here aims to investigate the differences between arterial wall models in the FSI simulation for a realistic geometry of aneurysm located in the aortic arch with physiologic boundary conditions. Furthermore, it is also investigated how different arterial wall models influence the blood flow field.

2 Materials and methods

2.1 Geometric reconstruction

Aortic arch geometry was obtained through the three-dimensional computed tomography (CT) reconstruction of a healthy 74-year-old patient. The procedure was approved by the Comitê de Ética em Pesquisa/Universidade Federal de Minas Gerais (CEP-UFGM) under process number CAAE02405712.5.1001.5149. A fusiform aneurysm was created to exceed the diameter of the aortic arch by at least 50%. Finally, the geometry of the arterial wall with a thickness of 2 mm was generated, which is within the physiological range measured in vitro [35]. Figure 1 shows the process of obtaining the geometries.

2.2 Mesh convergence test and numerical solution

For the fluid domain mesh, the convergence test was performed according to the ASME V&V 20 standard [36]. Velocity was monitored at four different points in the mesh. Each mesh was generated from the refinement of the previous one by a factor of 1.3 of the characteristic length (Eq. 1).

$$h = \left[\frac{1}{N} \sum_{i=1}^N \Delta V_i \right]^{1/3} \quad (1)$$

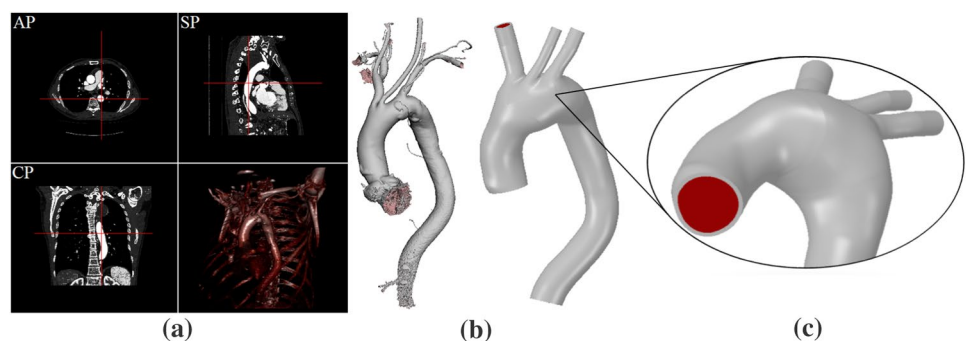
where ΔV_i is the volume of the i -th element and N is the total number of elements.

The strategy of refining the meshes was adopted until the grid convergence index (GCI) based on the relative error was less than 5%, or the GCI based on the absolute error was less than 10^{-3} at the four points analyzed in all time steps. The GCI is given by Eq. (2).

$$GCI_{\text{fine}}^{i,i+1} = \frac{FS \cdot e_a^{i,i+1}}{r_{i,i+1}^p - 1} \quad (2)$$

where $e_a^{i,i+1}$ is the relative or absolute error between meshes i and $i+1$, $r_{i,i+1}^p$ is the refinement factor, p is the apparent order

Fig. 1 Procedure for obtaining the geometries: **a** three-dimensional CT reconstruction, **b** resulting region of interest, **c** geometry resulting with zoom in the aneurysmal region. AP, axial plane; SP, sagittal plane; CP, coronal plane



of the method, and FS is the safety factor. $FS = 1.25$ was adopted [36]. After calculating five meshes, the expected value of the GCI was reached, and mesh number 4 was selected for the simulation.

For each mesh generated for the fluid domain, a mesh with a similar characteristic length was generated for the solid domain, to ensure that there was 100% coupling between the nodes at the mesh interface. The relative error of maximum principal stress (MPSS) was calculated at four different points in each mesh. A 1% limit for relative error was established to consider them converged.

The mesh selected for the fluid domain had 1,235,186 elements and 399,720 nodes and the mesh for the solid domain had 99,674 elements and 171,964 nodes. The mesh in the aneurysm area was finer, and the fluid domain mesh had 10 layers of refinement close to the wall, ensuring that the first layer had $y^+ < 1$ throughout the cardiac cycle. The test was performed for all arterial wall constitutive models used and it was found that the selected mesh is suitable for all.

In addition, a time step independence study was performed, where the time step was also reduced by a factor of 1.3 in each simulation until the velocity and MPSS at the same points of the mesh convergence test reached a difference under 5%, which resulted in a time step of 0.01 s. The cardiac cycle of 1.0 s (60 bpm) was considered. Five cardiac cycles were needed to eliminate unsteady regime effects and numerical instabilities. The results and analyzes were obtained considering the last cycle.

Coupling of the solid and fluid domains was performed by the System Coupling software (ANSYS 2019 R2). The solid model was discretized by the finite element method by ANSYS Mechanical 2019 R2, while the fluid model was discretized by the finite volume method by ANSYS Fluent 2019 R2. The residual value of 10^{-4} was adopted for the components of velocity, continuity, turbulence kinetic energy (k) and specific dissipation rate (ω) as a condition of convergence for the fluid domain. The Newton–Raphson method was used as the force convergence criterion for the solid domain. In this way, the residual used was 0.1% of the applied load. Two-way coupling was used. To assess the convergence of data transfers, the change in all values transferred between two successive iterations was reduced to a normalized value so that the root mean square (RMS) of 10^{-3} of this value was used as the convergence criterion.

For the momentum, k , and ω the second-order Upwind approximation method was adopted for the convection terms, and the central differencing scheme for the diffusive terms. In the discretization of the continuity equation, a procedure similar to that proposed by Rhie and Chow [37] was used to relate the velocity values on the face to the values stored in the centers of the cells. The Least Squares Method Cell-Based method was used for the solution of the gradients in the center of the cell. The second-order central differencing

scheme was adopted for cell face pressure interpolation in the discrete momentum equations. Backward second-order differences were used for temporal discretization.

At each time step, the first step consisted of coupling velocity and pressure by the coupled algorithm, converting the continuity equation into a pressure equation. A single system comprising the discrete equations of continuity and momentum [38] was solved using the coupled algebraic multigrid method (AMG) along with the incomplete lower upper (ILU) smoother. Then, the mass flow on each face was updated, and then the discrete equations of k and ω were solved by the AMG along with the Gauss–Seidel smoother. Finally, it was verified if convergence was reached, and if not, an update of all properties was performed to repeat the procedure.

2.3 Boundary conditions

For the fluid domain, the mass flow was defined as a boundary condition in the ascending aorta (inlet) and the pressure in the brachiocephalic trunk (BT), left common carotid artery (LCCA), left subclavian artery (LSA), and thoracic descending aorta (TDA). Figure 2a–b shows these boundary conditions along the cardiac cycle, which represents physiological flow conditions and were adapted from Alastruey et al. [39]. Figure 2c shows cut planes under which results were processed for analysis. At the inlet and outlets, a turbulent intensity of 5% was also adopted as a boundary condition. The non-slip condition was assumed in the wall.

For the solid domain, supports were imposed on the faces adjacent to the inlet and outlet sections to prevent displacements and rotations in all directions [40]. For the FSI interface, the fluid and solid displacements must be equal and the stresses in both domains must be in equilibrium.

2.4 Governing equations

The blood was assumed to be incompressible, so the continuity and momentum equations become Eqs. (3) and (4), respectively:

$$\nabla \cdot \mathbf{u} = 0 \quad (3)$$

$$\rho_f \left(\frac{\partial \mathbf{u}}{\partial t} + (\nabla \cdot \mathbf{u}) \cdot \mathbf{u} \right) = -\nabla p + \nabla \tau \quad (4)$$

where ρ_f is the blood density, \mathbf{u} is the velocity vector, p is the pressure, t is the instant of time and τ is the viscous stresses tensor, which is given by:

$$\tau = 2\mu \mathbf{D} \quad (5)$$

where \mathbf{D} is the strain rate tensor and μ is blood viscosity. The rheological model used was the Carreau, which is a widely

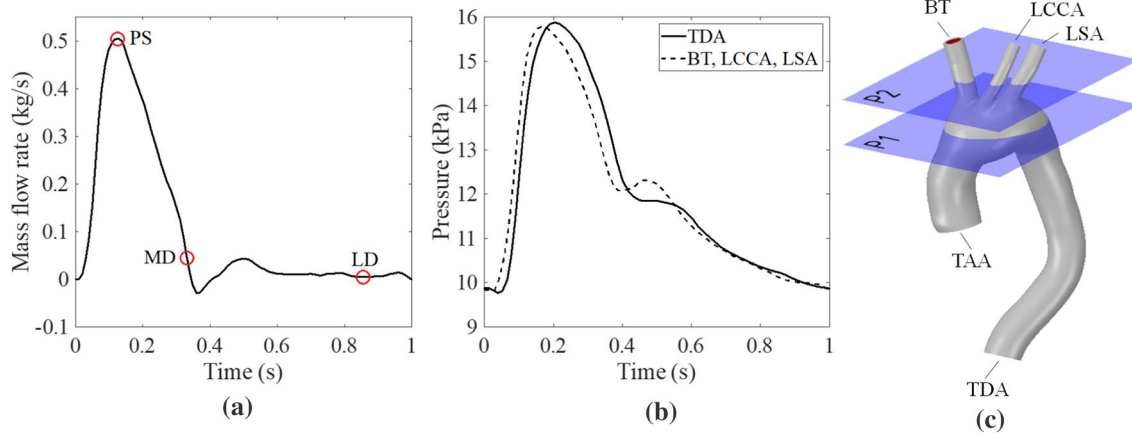


Fig. 2 Boundary conditions of the fluid domain: **a** mass flow rate waveform, **b** pulse pressure wave, **c** cutting planes used to analyze results in the aortic arch and branches. TDA, thoracic descending

aorta; TB, brachiocephalic trunk; LCCA, left common carotid artery; LSA, left subclavian artery; PS, peak systole; MD, maximum acceleration; LD, late diastole

used model for blood flow applications capable of modeling shear-thinning behavior [15, 18, 25, 41]. The viscosity for the Carreau model is given by:

$$\mu = \mu_{\infty} + (\mu_0 - \mu_{\infty}) (1 + (\lambda \dot{\gamma})^2)^{\frac{n-1}{2}} \tag{6}$$

where $\dot{\gamma}$ is the shear rate, μ_0 is the zero-shear stress viscosity, μ_{∞} is the infinite shear stress viscosity, a is the Yasuda constant, λ is a time constant and n is the power law. The values used were $\mu_0 = 0.056$ Pa s, $\mu_{\infty} = 0.0035$ Pa s, $\lambda = 3.313$ s and $n = 0.03568$ [42]. The value of 1060 kg/m^{-3} was adopted [43] for blood density.

Aneurysms can induce turbulence due to sudden geometric changes [44, 45]. Even at low Reynolds numbers (Re), flow pulsation can destabilize the flow and initiate a transition to turbulence [44]. Thus, the flow was assumed to be turbulent and the turbulence model $k-\omega$ SST—shear-stress transport- was adopted.

The Lagrangian coordinate system was adopted for the solid domain:

$$\nabla \cdot \boldsymbol{\sigma}_s = \rho_s \dot{\mathbf{u}}_g \tag{7}$$

where $\boldsymbol{\sigma}_s$ is the solid stress tensor, ρ_s is the density of the arterial wall and $\dot{\mathbf{u}}_g$ is the local acceleration vector.

The difficulty in obtaining data in the literature on the mechanical properties of the artery is due to the arterial sampling process itself [32, 46]. Furthermore, the arterial nature can cause the parameters to vary over a wide range depending on the person's health, age, gender, etc. The isotropic linear elastic model (LE1) was adopted with elastic modulus $E = 1$ MPa and Poisson coefficient $\nu = 0.49$ [40, 47]. A stiffer isotropic linear elastic model (LE2) was also adopted, with elastic modulus $E = 2$ MPa [48]. The

two-terms Yeoh model (Eq. (8)) [49] was adopted for the isotropic hyperelastic model.

$$W = C_{10} (\bar{I}_1 - 3) + C_{20} (\bar{I}_1 - 3)^2 \tag{8}$$

where \bar{I}_1 is the first deviatoric strain invariant. The material constants, $C_{10} = 0.174$ MPa and $C_{20} = 1.881$ MPa, were adopted from Raghavan and Vorp [49].

Finally, the Holzapfel model [9] was adopted for the anisotropic hyperelastic model, whose energy density function is given by:

$$W = \frac{C_{10}}{2} (\bar{I}_1 - 3) + \frac{k_1}{2k_2} \sum_{i=4,6} \left(e^{k_2 (\bar{I}_i - 1)^2} - 1 \right) \tag{9}$$

where \bar{I}_4 and \bar{I}_6 are the pseudo-invariants of the Green-Cauchy tensor, and k_1 and k_2 the constants of the material.

The material parameters for the Holzapfel constitutive model were calculated based on Huh et al. [50], which relates these parameters according to the patient's age. The maximum values of the parameters of the methodology proposed by Huh et al. [50] were adopted because the aneurysm walls are stiffer than healthy ones [51]. The resulting values were: $C_{10} = 0.218$ MPa, $k_1 = 0.16437$ MPa and $k_2 = 4.1787$.

2.5 Verification of numerical simulation

The Holzapfel arterial wall model was simulated in a healthy aorta to verify the simulation, comparing it to other results in the literature. The same geometry described was used, however, the aneurysm was not generated. The methodology used in this simulation was the same as the aneurysmal case. The outflow in the brachiocephalic trunk resulting from the numerical simulation was compared with the results

of measurements by in vivo magnetic resonance imaging (MRI) performed by Olufsen et al. [52] and Boccadifuoco et al. [53].

3 Results and discussion

3.1 Solid domain

Hemodynamics plays a crucial role in the physiological and pathological changes of the cardiovascular system [40].

From a biomechanical perspective, the aneurysm ruptures or dissects when the stresses acting on the arterial wall exceed the ultimate tensile strength according to some suitable failure criterion. So that the analysis of wall stress is a better rupture predictor than the local diameter of the aneurysm [7, 15]. The failure criterion of MPSS was used in this work.

Figure 3 shows the average and peak of MPSS, displacement, and maximum principal strain (MPS) in the two planes of Fig. 2c for the four arterial wall models. At the peak of systole (PS), the MPSS of the Yeoh model was higher than other models, which was also verified by Cosentino et al.

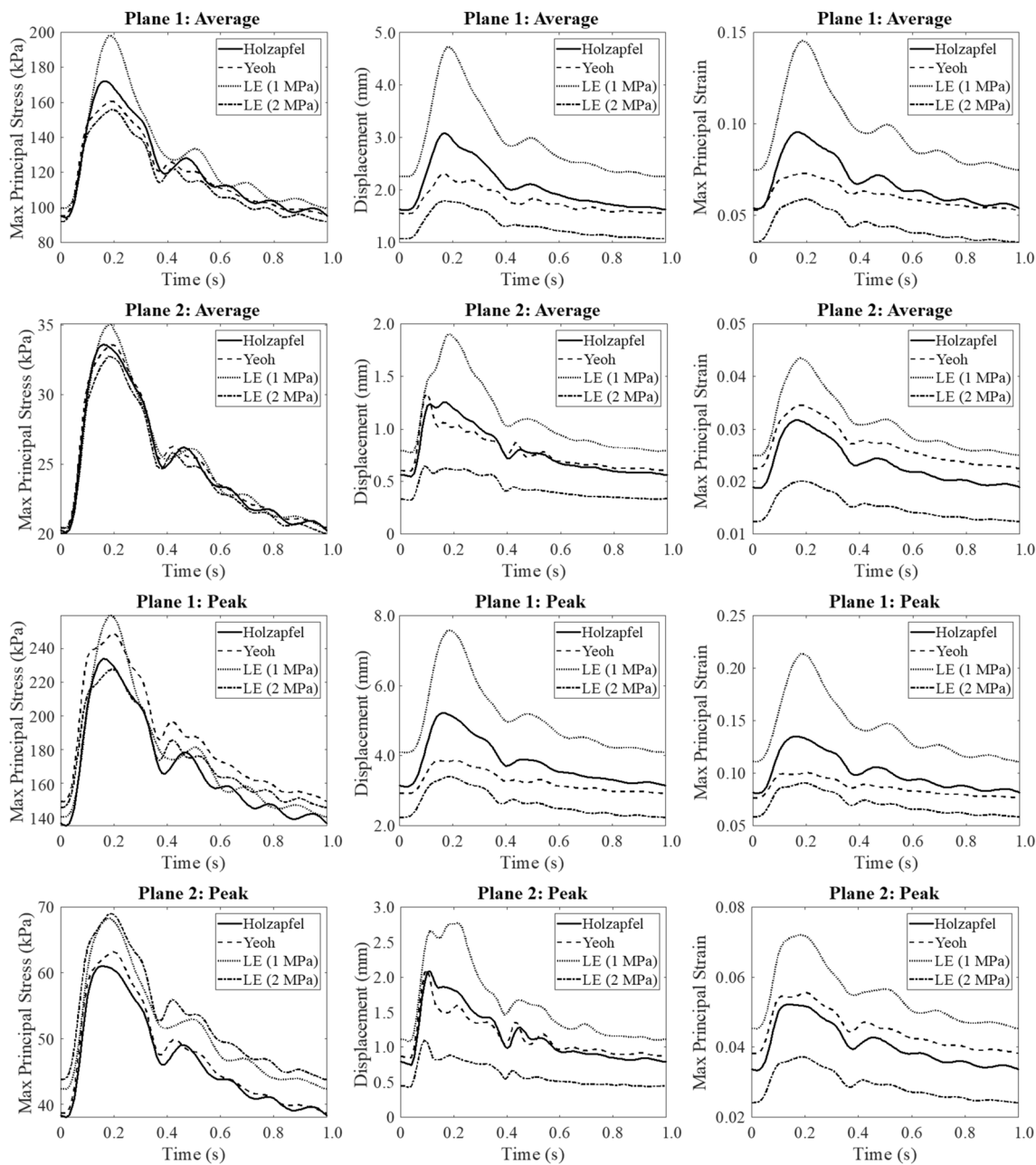


Fig. 3 Maximum principal stress, displacement, and maximum principal strain in planes P1 and P2

[32] in the simulation of aneurysms in the ascending aorta, comparing the Yeoh model with the LE and Fung models. Generally, it was observed that the LE1 model tended to overestimate the hyperelastic models, while the LE2 model tended to underestimate them in MPSS, displacement, and MPS. Comparing the two hyperelastic models, it is interesting to note that the peak of MPSS in P1 was smaller in the anisotropic model than in the isotropic model, however, the displacement and MPS were higher in the anisotropic model, possibly due to the greater stiffness of this model.

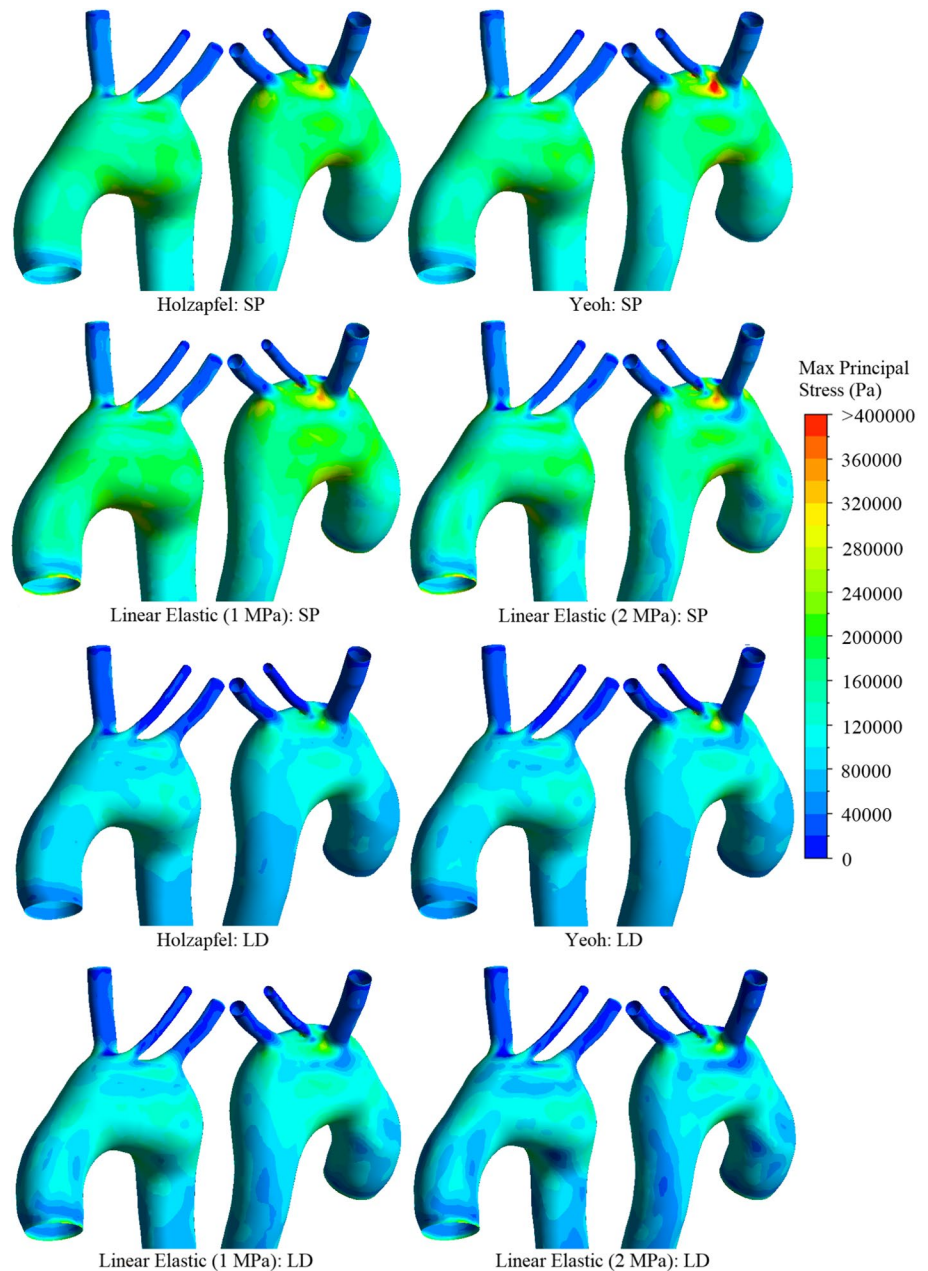
In the diastole phase, all perspectives tended to be similar because the blood ejection was low, therefore, the pressure on the wall, mechanical efforts, and displacement were also

smaller, resulting in a similar behavior of the hemodynamics field and the mechanical response of the wall in all models.

Figure 4 shows MPSS contours on the inner arterial wall of the vessel at PS and late diastole (LD).

Stress in the aneurysm wall was non-uniform, greater than in other regions of the aorta, and quantitatively close to those found by Campobasso et al. [15] in the aneurysms of the ascending aorta. The peak of MPSS occurred at the junction of supra-aortic branches with aortic arch, close to the brachiocephalic trunk in the PS and they were: 356,459 Pa, 506,405 Pa, 384,592 Pa, and 395,674 Pa for the Holzapfel, Yeoh, LE1, and LE2 models respectively. However, this region had a limited movement that prevented large

Fig. 4 Maximum principal stress in PS and LD on the inner wall of the aortic arch



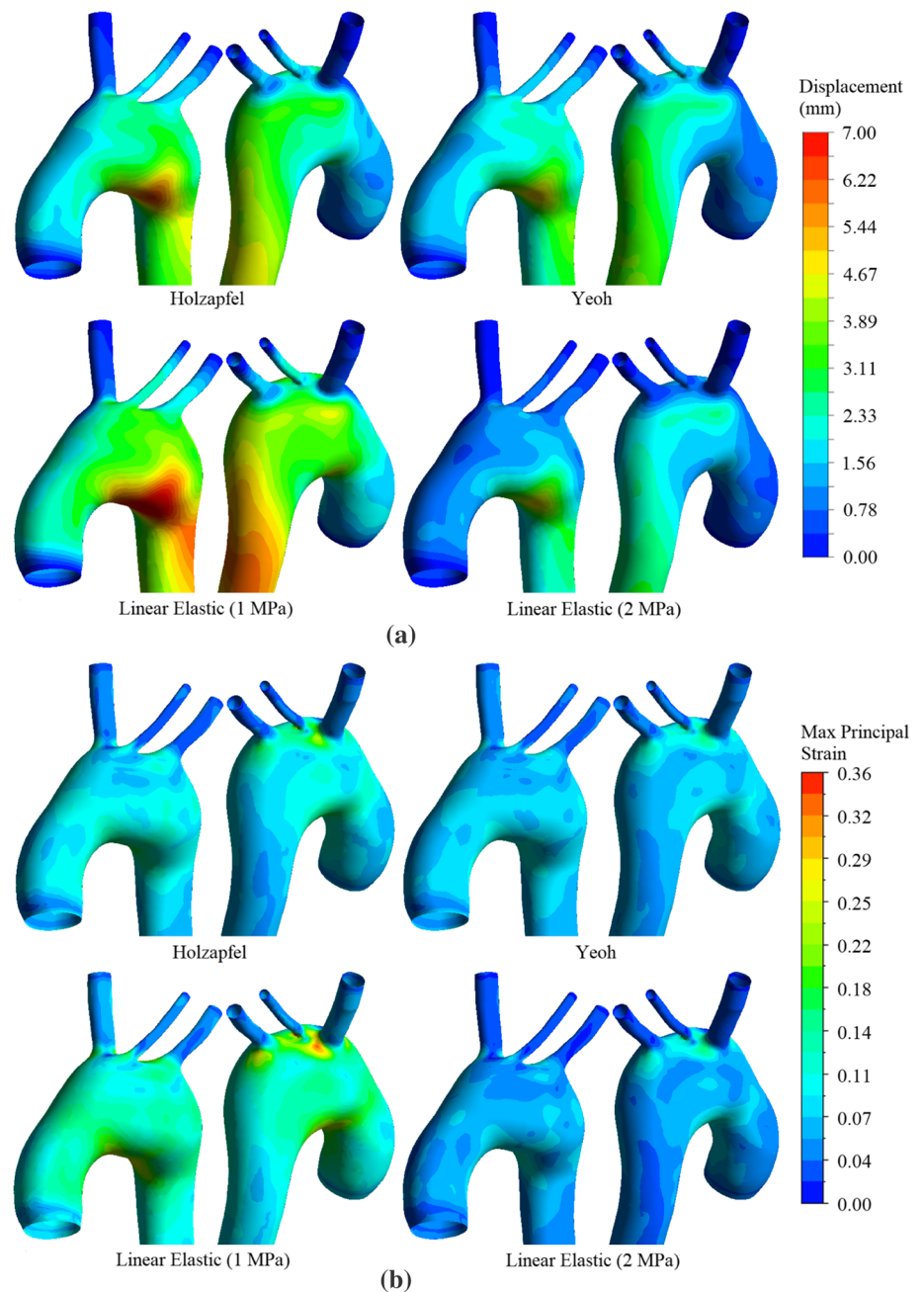
displacements as can be seen in Fig. 5. In fact, according to De Galarreta et al. [54], the curvature of the aneurysm correlates better with the peak stress than the local diameter of the aneurysm.

The incorporation of anisotropy in the aneurysmal tissue appears to increase the MPSS acting on the arterial wall of AAA [55, 56], having it already been shown that the average peak wall stress between the isotropic and anisotropic models is statistically significant [57]. In the study developed here, the isotropic hyperelastic model and the anisotropic hyperelastic model exhibited the highest and lowest peaks of MPSS, respectively, however, in the aneurysm sac region,

the anisotropic hyperelastic model showed a higher MPSS than the isotropic hyperelastic model.

Wall distensibility is also related to the rupture process. Degeneration of the aneurysmal wall is related to increased stiffness and therefore decreased extensibility, mainly in the circumferential direction [12]. Thus, stiffer TAA have a significantly increased risk of rupture [15]. According to Fig. 5, although the peak wall stress had been higher in the Yeoh model, the peak strain and displacement in this model were low. The peak stress of LE1 model was 24.05% lower than that of Yeoh model, however, the peak displacement and peak strain of LE1

Fig. 5 Contours of the inner wall of the aortic arch in PS: **a** displacement, **b** maximum principal strain



model were 62.73% and 123.96% higher, respectively. This fact was probably due to the nonlinear response of the Yeoh hyperelastic model, while in the LE1 model the response is linear. Furthermore, the lower displacements found in the LE1 model in relation to the Yeoh model are in agreement with Bilgi and Atalık [18], who compared these models for abdominal aortic aneurysm (AAA). The lower displacement that occurred in the stiffer models studied here, combined with the higher MPSS observed in these models, may be indicative of an overestimation of the risk of aneurysm rupture. Therefore, the Yeoh model was the one that most overestimated the risk of rupture.

Figure 6a-b shows contours of MPSS and MPS, respectively, and Fig. 6c shows the displacement of the inner wall of P1 at the PS relative to the beginning of the cardiac cycle. The highest values of MPSS and MPS at P1 occurred in the inner wall in the posterior part of the aneurysm, but the greatest displacement of the wall occurs in the anterior part of the aneurysm, probably due to the curvature of the aortic arch that favored this movement. The LE1 model was the only one that showed considerable movement in the posterior region of the aneurysm.

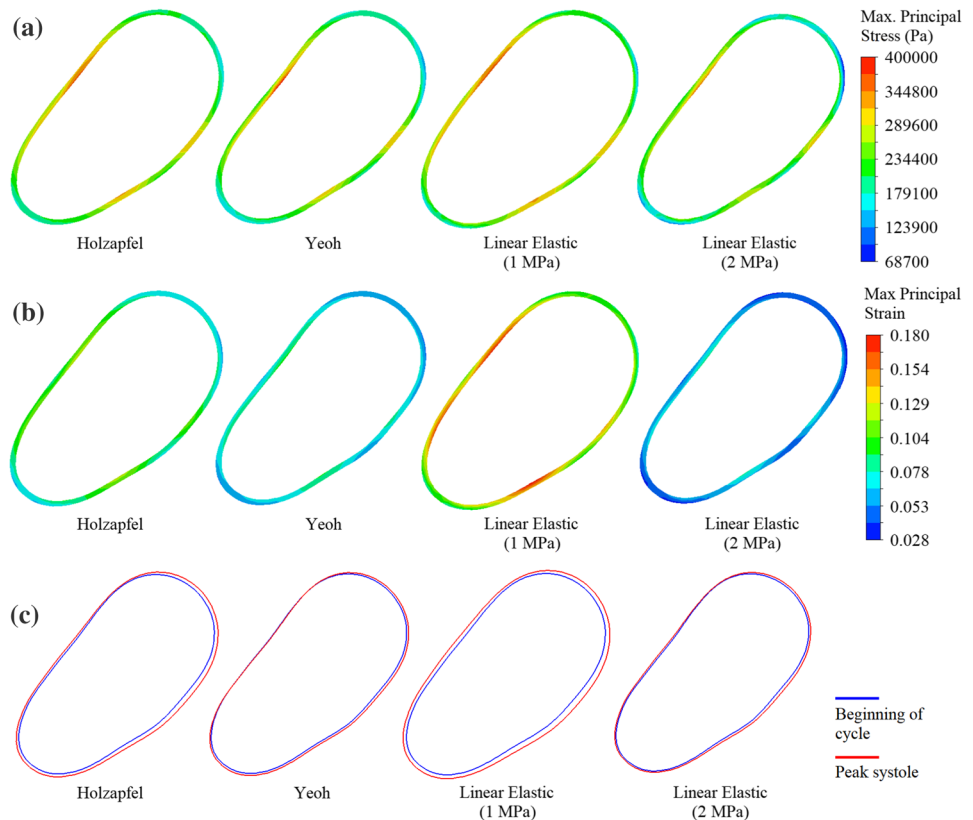
3.2 Fluid domain

Figure 7a–f shows the average values of velocity, hydraulic diameter, viscosity, Re, Womersley number (Wo), and turbulent kinetic energy (TKE) overtime at P1. Figure 7g shows the variation of the lumen area in P1 in relation to the pressure throughout the cardiac cycle. Figure 7h-i shows the average values of pressure and WSS at the wall. Re and Wo were calculated on the basis of hydraulic diameter and the average of other variables in P1.

Although all models had similar pressure on the wall throughout the cardiac cycle, the mechanical behavior of the arterial wall was different in each model, which was reflected in the hemodynamic behavior. Figure 7b and g show changes in hemodynamics due to the different forms of expansion and compression of wall in each model. In addition to stretching more, the less stiff models, i.e., LE1 and Holzapfel, presented the movement of dilating and compressing faster than the stiffer models. As shown in Fig. 7g, different hysteresis behaviors were observed at PS in each model.

The Holzapfel, Yeoh, LE1, and LE2 models exhibited similar percent maximum viscosity variation throughout the cycle: 0.6801%, 0.6582%, 0.6888%, and 0.6852%, respectively. The valley in the viscosity graph (Fig. 7c) constitutes the moment of the highest strain rate, which occurred at

Fig. 6 Cross section of the aortic wall in relation to P1 at the moment of PS: **a** maximum principal stress, **b** maximum principal strain, **c** inner wall contour showing displacement in relation to the beginning of the cardiac cycle



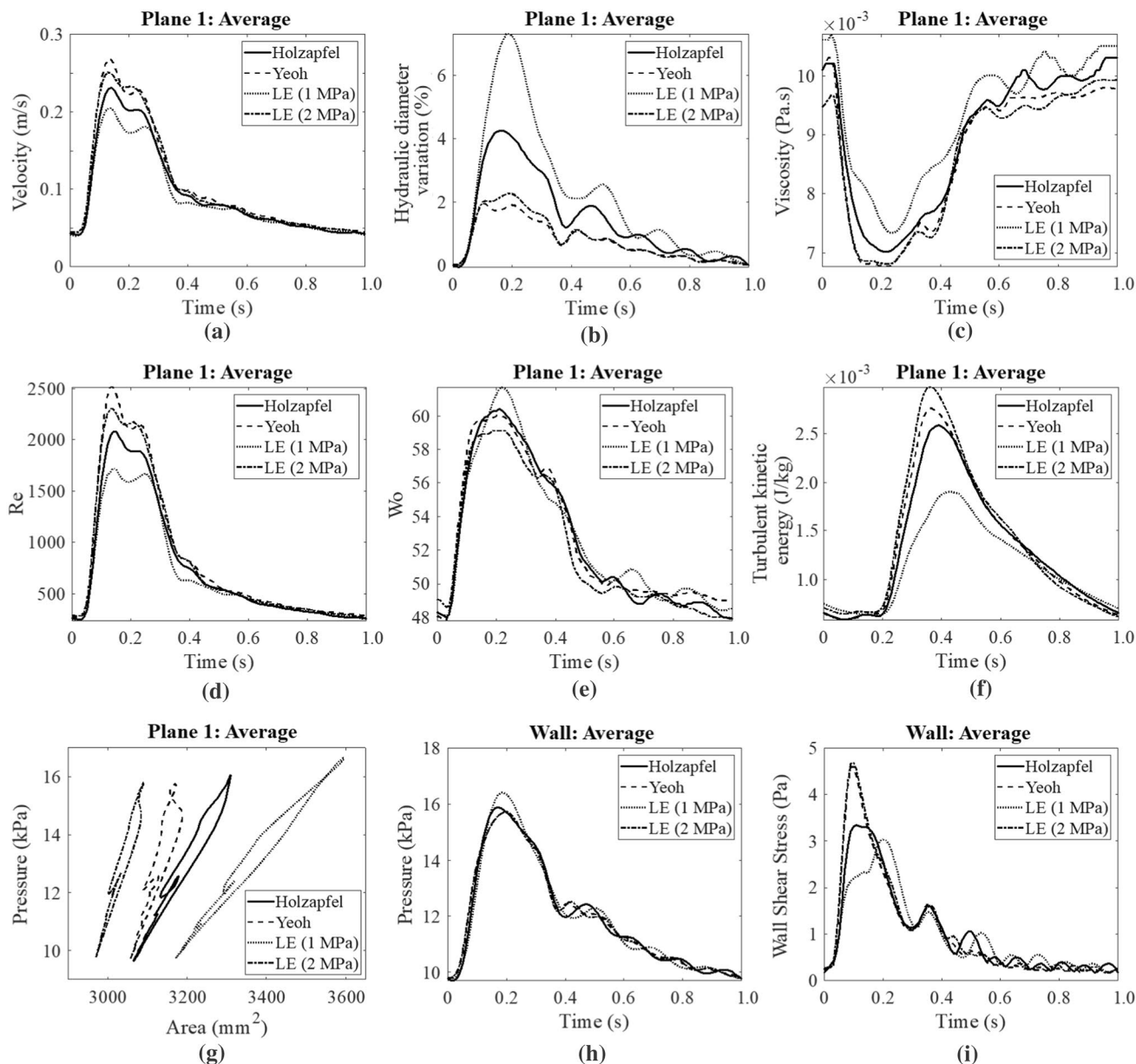


Fig. 7 a Average velocity at P1, b percentage change in diameter at P1, c average viscosity at P1 d Re in P1, e Wo in P1, f average turbulence kinetic energy in P1, g Lumen area variation at P1 in relation to pressure, h Lumen wall pressure, i WSS in the lumen wall

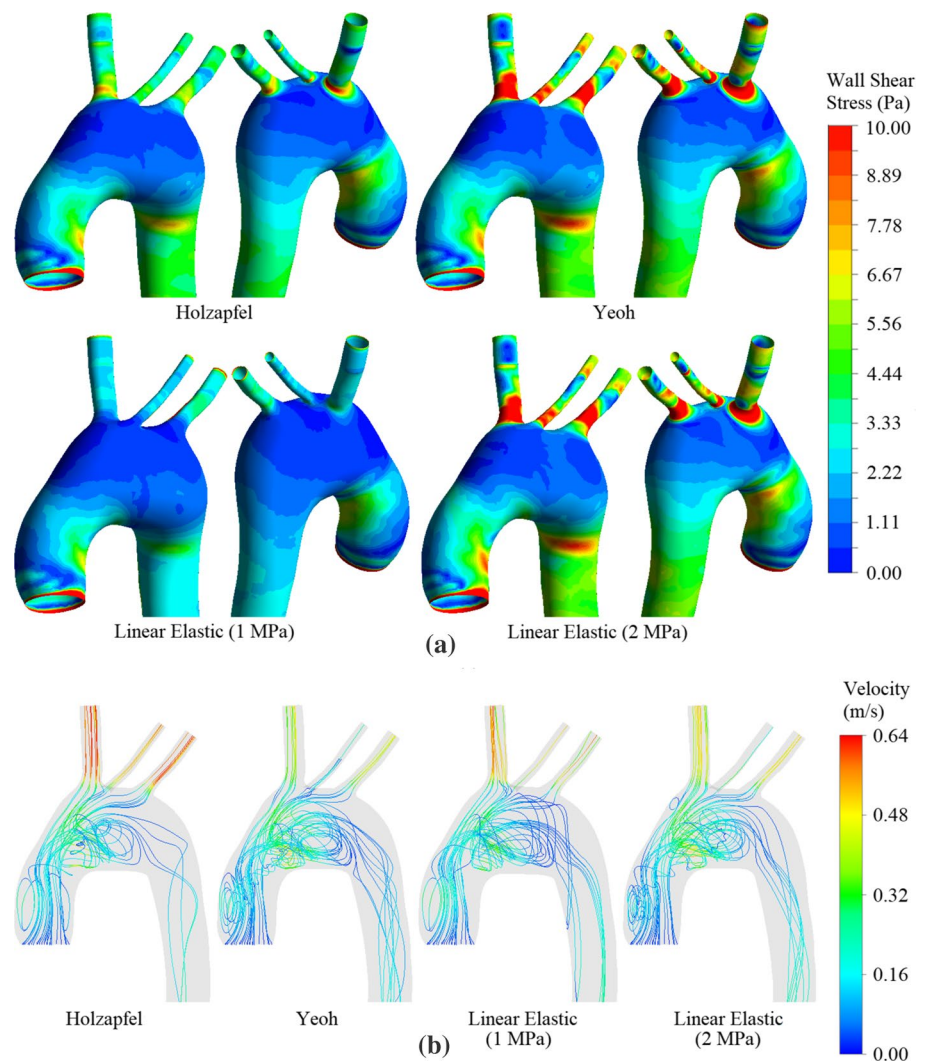
the systole, and it is in agreement with the shear-thinning rheological behavior of blood. The less stiff models showed the highest viscosity throughout the cycle, which indicates that the viscosity tends to be higher with the increase in the blood vessel.

WSS contours on the lumen wall at the PS and streamlines at the moment of maximum deceleration (MD) are shown in Fig. 8.

High WSS values were identified in the supra-aortic branches, due to the increase in velocity and velocity gradient that in turn were caused by the small diameter of

these arteries, which was also shown by Savabi et al. [40] and Simão et al. [25]. Other points of high WSS were observed at the beginning of the arch curvature in the ascending aorta and at the end of the arch curvature in the descending aorta, due to the change in flow direction and the impact of flow jet on the aortic wall, which agrees with Simão et al. [25] and Condemi et al. [58]. High WSS has been associated with degradation of the aortic wall in aneurysms, at the same time, it may be associated with an increase in ultimate tensile strength [23].

Fig. 8 **a** WSS in PS, **b** streamlines in MD instant



On the other hand, low WSS is associated with ILT formation and atherosclerosis [24–27]. Variations in arterial wall stiffness, extensibility, and degree of anisotropy are associated with the presence of ILT [7, 59]. The ILT formation mechanism in aneurysms, although still unknown, may be related to hemodynamics, specifically the presence of persistent vortices in the aneurysmal sac that leads to trapping of thrombus-causing blood particles that can be activated by shear stress [59]. From a hemodynamic perspective, recirculation results in a reduction in WSS [25, 60], which in turn can contribute to vessel weakening and degeneration, promoting aneurysm growth [29, 45, 60]. The aneurysmal sac was a region that favored recirculation, especially in the diastole, where the velocity was low. Consequently, the less stiff models, which exhibited greater distension and, therefore, larger aneurysmal sacs, favored recirculation and may overestimate ILT formation and indirectly also overestimated aneurysm growth.

If a value of 2 Pa is assumed as the minimum threshold for maintaining the arterial vascular structure without endothelial degeneration [18, 61], the area of the aneurysm suffered the most damage. Additionally, it was observed a special case of the LE1 model, which was the only one that presented low WSS at the junction of supra-aortic branches with aortic arch, indicating possible degeneration and risk of atherosclerosis in a region that was also verified high wall stress.

The highest TKE value (Fig. 7f) occurred at the flow deceleration phase. This fact was due to the deceleration of the flow having generated regions of recirculation and the formation of vortices in the aneurysmal sac. LE2 and Yeoh models presented higher TKE, because stiffer aneurysmal walls prevent energy dissipation, increasing TKE in the vortex region [22, 62], contributing to an overestimation of the WSS [22]. Finally, Fig. 8b shows that the recirculation tended to be located in the lower part of the aneurysmal

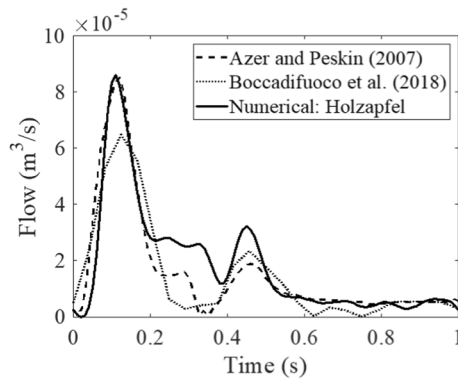


Fig. 9 Verification of the Holzapfel model simulation in a healthy geometry

sac, which coincides with high values of MPSS and MPS on the wall, which was also verified by Ong et al. [63].

3.3 Verification of numerical simulation and limitations

Figure 9 shows the results of the Holzapfel model in a healthy geometry compared to experimental studies.

Based on the most sophisticated model studied here, the Holzapfel model, in a geometry of the healthy aortic arch, it was possible to satisfactorily verify the simulation with experimental data available in the literature. Figure 9 shows that the flow behavior followed the qualitative trend of experimental studies on the brachiocephalic trunk. It can be noted that there were quantitative differences even in experimental studies due to differences in patient-specific natural conditions.

The study carried out here has some limitations, although it does not preclude the comparison and discussion of the aortic wall models studied. The boundary conditions for the fluid domain were adapted from data in the literature on the aorta in healthy conditions, but the presence of aneurysms may cause some variation in these conditions. In the solid domain, it is still necessary to study and understand how the contact of the aorta with other organs and tissues reflects on the supports to be adopted as a boundary condition. The lack of specific aortic arch data for arterial wall models is another limitation of the study. Finally, the mechanical response variables were used to detect critical points for ILT formation, dissection, and rupture, so that in the next stages of the project, specific models to analyze ILT formation and dissection will be used.

4 Conclusion

Knowledge of the mechanical response of the arterial wall and its interaction with hemodynamics is clinically important as a tool for predicting aneurysm rupture since the analysis of stresses and disturbances in the flow field are better predictors of rupture than the diameter and growth rate of the aneurysm. Furthermore, mechanical and flow field variables provide important information for the detection of other typical aneurysm pathologies, such as ILT formation, atherosclerosis, and aneurysm growth. In this way, the real-life applications of the fluid-structural numerical models used in this work encompass, among others, the prediction of the rupture, dissection, and development of other pathologies associated with aneurysms through detailed information that is not possible in real-life. In addition, the models provide an understanding of the movement of the arterial wall for the use of clinical devices, implantation of endoprostheses, and surgeries.

The work carried out here shows a comparison of different arterial wall models available in the literature for numerical fluid–structure simulation of an aortic arch aneurysm. The mechanical behavior of each constitutive model and how this behavior interferes with the flow field were shown. Less stiff arterial wall models, such as the LE1, were found to have greater growth of the aneurysmal sac that provides more space for recirculation, reducing WSS, which can indirectly indicate an overestimation of ILT formation, as well as the aneurysm growth. More than that, less stiff models dissipated more energy in the aneurysm wall, presenting lower TKE values. From a biomechanical perspective, stiffer models presented a lower MPSS than the other models in the aneurysm area, but the peak of MPSS was higher, especially in the isotropic hyperelastic model, which may overestimate the risk of rupture.

The incorporation of specific ILT formation and dissection models in future works may establish a relationship with the variables analyzed here, providing a more complete analysis of the aortic wall models studied.

Acknowledgements The authors would like to thank Conselho Nacional de Desenvolvimento Científico e Tecnológico—CNPq (312982/2017-8). This study was financed in part by the Coordenação de Aperfeiçoamento de Pessoal de Nível Superior—Brasil (CAPES)—Finance Code 001.

Funding This study was financed in part by the Coordenação de Aperfeiçoamento de Pessoal de Nível Superior—Brasil (CAPES)—Finance Code 001.

Availability of data and material Not applicable.

Code availability Not applicable.

Declarations

Conflict of interest On behalf of all authors, the corresponding author states that there is no conflict of interest.

Ethics approval Aortic arch geometry was obtained through the three-dimensional computed tomography (CT) reconstruction of a healthy 74-year-old patient. The procedure was approved by the Research Ethics Committee/Federal University of Minas Gerais (CEP-UFGM) under process number CAAE02405712.5.1001.5149.

References

- eMelo RG, Duarte GS, Lopes A, Alves M, Caldeira D, eFernandes RF, Pedro LM (2021) Incidence and prevalence of thoracic aortic aneurysms: a systematic review and meta-analysis of population-based studies. *Semin Thoracic Surg*. <https://doi.org/10.1053/j.semtcvs.2021.02.029>
- Elhelali A, Hynes N, Devane D, Sultan S, Kavanagh EP, Morris L, Veerasingam D, Jordan F (2021) Hybrid repair versus conventional open repair for thoracic aortic arch aneurysms. *Cochrane Database Syst Rev*. <https://doi.org/10.1002/14651858.CD012923.pub2>
- Bashir M, Harky A, Bilal H (2019) Is there a prospect for hybrid aortic arch surgery? *Gen Thorac Cardiovasc Surg* 67:132–136. <https://doi.org/10.1007/s11748-018-0940-z>
- Holzapfel GA, Ogden RW (2018) Biomechanical relevance of the microstructure in artery walls with a focus on passive and active components. *Am J Physiol Heart Circ Physiol* 315:H540–H549. <https://doi.org/10.1152/ajpheart.00117.2018>
- Amabili M, Asgari M, Breslavsky ID, Franchini G, Giovannello F, Holzapfel GA (2021) Microstructural and mechanical characterization of the layers of human descending thoracic aortas. *Acta Biomater* 134:401–421. <https://doi.org/10.1016/j.actbio.2021.07.036>
- Kobielarz M (2020) Effect of collagen fibres and elastic lamellae content on the mechanical behaviour of abdominal aortic aneurysms. *Acta Bioeng Biomech* 22:9–21. <https://doi.org/10.37190/ABB-01580-2020-02>
- Haller SJ, Azarbal AF, Rugonyi S (2020) Predictors of abdominal aortic aneurysm risks. *Bioengineering* 7:1–19. <https://doi.org/10.3390/bioengineering7030079>
- Gasser TC, Ogden RW, Holzapfel GA (2006) Hyperelastic modelling of arterial layers with distributed collagen fibre orientations. *J R Soc Interface* 3:15–35. <https://doi.org/10.1098/rsif.2005.0073>
- Holzapfel GA, Gasser TC, Ogden RW (2000) A new constitutive framework for arterial wall mechanics and a comparative study of material models. *J Elast* 61:1–48. <https://doi.org/10.1023/A:1010835316564>
- Duprey A, Trabelsi O, Vola M, Favre JP, Avril S (2016) Biaxial rupture properties of ascending thoracic aortic aneurysms. *Acta Biomater* 42:273–285. <https://doi.org/10.1016/j.actbio.2016.06.028>
- Pierce DM, Maier F, Weisbecker H, Viertler C, Verbrugge P, Famaey N, Fourneau I, Herijgers P, Holzapfel GA (2015) Human thoracic and abdominal aortic aneurysmal tissues: damage experiments, statistical analysis and constitutive modeling. *J Mech Behav Biomed Mater* 41:92–107. <https://doi.org/10.1016/j.jmbbm.2014.10.003>
- Vande Geest JP, Sacks MS, Vorp DA (2006) The effects of aneurysm on the biaxial mechanical behavior of human abdominal aorta. *J Biomech* 39:1324–1334. <https://doi.org/10.1016/j.jbiomech.2005.03.003>
- Teng Z, Feng J, Zhang Y, Huang Y, Sutcliffe MP, Brown AJ, Jing Z, Gillard JH, Lu Q (2015) Layer-and direction-specific material properties, extreme extensibility and ultimate material strength of human abdominal aorta and aneurysm: a uniaxial extension study. *Ann Biomed Eng* 43:2745–2759. <https://doi.org/10.1007/s10439-015-1323-6>
- Niestrawska JA, Regitnig P, Viertler C, Cohnert TU, Babu AR, Holzapfel GA (2019) The role of tissue remodeling in mechanics and pathogenesis of abdominal aortic aneurysms. *Acta Biomater* 88:149–161. <https://doi.org/10.1016/j.actbio.2019.01.070>
- Campobasso R, Condemi F, Viallon M, Croisille P, Campisi S, Avril S (2018) Evaluation of peak wall stress in an ascending thoracic aortic aneurysm using FSI simulations: effects of aortic stiffness and peripheral resistance. *Cardiovasc Eng Technol* 9:707–722. <https://doi.org/10.1007/s13239-018-00385-z>
- Wilson KA, Lee AJ, Hoskins PR, Fowkes FG, Ruckley CV, Bradbury AW (2003) The relationship between aortic wall distensibility and rupture of infrarenal abdominal aortic aneurysm. *J Vasc Surg Cases* 37:112–117. <https://doi.org/10.1067/mva.2003.40>
- Haller SJ, Crawford JD, Courchaine KM et al (2018) Intraluminal thrombus is associated with early rupture of abdominal aortic aneurysm. *J Vasc Surg* 67:1051–1058.e1. <https://doi.org/10.1016/j.jvs.2017.08.069>
- Bilgi C, Atalik K (2019) Numerical investigation of the effects of blood rheology and wall elasticity in abdominal aortic aneurysm under pulsatile flow conditions. *Biorheology* 56:51–71. <https://doi.org/10.3233/BIR-180202>
- Rahmani S, Jarrahi A, Saed B et al (2019) Three-dimensional modeling of Marfan syndrome with elastic and hyperelastic materials assumptions using fluid-structure interaction. *Biomed Mater Eng* 30:255–266. <https://doi.org/10.3233/BME-191049>
- Schmidt T, Pandya D, Balzani D (2015) Influence of isotropic and anisotropic material models on the mechanical response in arterial walls as a result of supra-physiological loadings. *Mech Res Commun* 64:29–37. <https://doi.org/10.1016/j.mechrescom.2014.12.008>
- de Gelidi S, Bucchi A (2019) Comparative finite element modelling of aneurysm formation and physiologic inflation in the descending aorta. *Comput Methods Biomech Biomed Engin* 22:1197–1208. <https://doi.org/10.1080/10255842.2019.1650036>
- Lin S, Han X, Bi Y, Ju S, Gu L (2017) Fluid-structure interaction in abdominal aortic aneurysm: effect of modeling techniques. *Biomed Res Int* 2017:1–11. <https://doi.org/10.1155/2017/7023078>
- Salmasi MY, Pirola S, Sasidharan S, Fisichella SM, Redaelli A, Jarral OA, O'Regan DP, Oo AY, Moore JE Jr, Xu XY, Athanasiou T (2021) High wall shear stress can predict wall degradation in ascending aortic aneurysms: an integrated biomechanics study. *Front Bioeng Biotechnol* 9:750656. <https://doi.org/10.3389/fbioe.2021.750656>
- Harky A, Sokal PA, Hasan K, Papaleontiou A (2021) The aortic pathologies: how far we understand it and its implications on thoracic aortic surgery. *Braz J Cardiovasc Surg*. <https://doi.org/10.21470/1678-9741-2020-0089>
- Simão M, Ferreira JM, Tomas AC, Fragata J, Ramos H (2017) Aorta ascending aneurysm analysis using CFD models towards possible anomalies. *Fluids* 2:1–15. <https://doi.org/10.3390/fluid2020031>
- Lozowy RJ, Kuhn DCS, Ducas AA, Boyd AJ (2017) The relationship between pulsatile flow impingement and intraluminal thrombus deposition in abdominal aortic aneurysms. *Cardiovasc Eng Technol* 8:57–69. <https://doi.org/10.1007/s13239-016-0287-5>
- Boyd AJ, Kuhn DCS, Lozowy RJ, Kulbisky GP (2016) Low wall shear stress predominates at sites of abdominal aortic aneurysm rupture. *J Vasc Surg* 63:1613–1619. <https://doi.org/10.1016/j.jvs.2015.01.040>

28. Yeh HH, Rabkin SW, Grecov D (2018) Hemodynamic assessments of the ascending thoracic aortic aneurysm using fluid-structure interaction approach. *Med Biol Eng Comput* 56:435–451. <https://doi.org/10.1007/s11517-017-1693-z>
29. Zhu C, Leach JR, Wang Y, Gasper W, Saloner D, Hope MD (2020) Intraluminal thrombus predicts rapid growth of abdominal aortic aneurysms. *Radiology* 294:707–713. <https://doi.org/10.1148/radiol.2020191723>
30. Liang L, Liu M, Martin C, Sun W (2018) A deep learning approach to estimate stress distribution: a fast and accurate surrogate of finite-element analysis. *J R Soc Interface* 15:20170844. <https://doi.org/10.1098/rsif.2017.0844>
31. Liu M, Liang L, Sun W (2017) A new inverse method for estimation of in vivo mechanical properties of the aortic wall. *J Mech Behav Biomed Mater* 72:148–158. <https://doi.org/10.1016/j.jmbbm.2017.05.001>
32. Cosentino F, Agnese V, Raffa GM et al (2019) On the role of material properties in ascending thoracic aortic aneurysms. *Comput Biol Med* 109:70–78. <https://doi.org/10.1016/j.combiomed.2019.04.022>
33. Fereidoonhezad B, O'Connor C, McGarry JP (2020) A new anisotropic soft tissue model for elimination of unphysical auxetic behaviour. *J Biomech* 111:110006. <https://doi.org/10.1016/j.jbiomech.2020.110006>
34. Nolan DR, Gower AL, Destrade M, Ogden R, McGarry J (2014) A robust anisotropic hyperelastic formulation for the modelling of soft tissue. *J Mech Behav Biomed Mater* 39:48–60. <https://doi.org/10.1016/j.jmbbm.2014.06.016>
35. García-Herrera CM, Celentano DJ (2013) Modelling and numerical simulation of the human aortic arch under in vivo conditions. *Biomech Model Mechanobiol* 12:1143–1154. <https://doi.org/10.1007/s10237-013-0471-6>
36. McHale MP, Friedman JR, Karian J (2009) Standard for verification and validation in computational fluid dynamics and heat transfer. *Am Soc Mech Eng ASME* 2009:20
37. Rhie CM, Chow WL (1983) Numerical study of the turbulent flow past an airfoil with trailing edge separation. *AIAA J* 21:1525–1532. <https://doi.org/10.2514/3.8284>
38. Shin JR, Kim TW (2021) Enhanced pressure based coupled algorithm to combine with pressure–velocity–enthalpy for all Mach number flow. *Int J Aeronaut* 22:489–501. <https://doi.org/10.1007/s42405-020-00337-9>
39. Alastruey J, Xiao N, Fok H, Schaeffter T, Figueroa CA (2016) On the impact of modelling assumptions in multi-scale, subject-specific models of aortic haemodynamics. *J R Soc Interface* 13:20160073. <https://doi.org/10.1098/rsif.2016.0073>
40. Savabi R, Nabaei M, Farajollahi S, Fatouree N (2020) Fluid structure interaction modeling of aortic arch and carotid bifurcation as the location of baroreceptors. *Int J Mech Sci* 165:105222. <https://doi.org/10.1016/j.ijmecsci.2019.105222>
41. Abbas Z, Imran M, Naveed M (2019) Hydromagnetic flow of a Carreau fluid in a curved channel with non-linear thermal radiation. *Therm Sci* 23(6):3379–3390. <https://doi.org/10.2298/TSCI171011077A>
42. Shibeshi SS, Collins WE (2005) The rheology of blood flow in a branched arterial system. *Appl Rheol* 15:398–405. <https://doi.org/10.1080/13632469.2015.1104754>
43. Galdi GP, Rannacher R, Robertson AM, Turek S (2008) Hemodynamical flows—modeling, analysis and simulation, 1st edn. Birkhäuser Verlag, Berlin
44. Vergara C, Le Van D, Quadrio M, Formaggia L, Domanin M (2017) Large eddy simulations of blood dynamics in abdominal aortic aneurysms. *Med Eng Phys* 47:38–46. <https://doi.org/10.1016/j.medengphy.2017.06.030>
45. Numata S, Itatani K, Kanda K et al (2016) Blood flow analysis of the aortic arch using computational fluid dynamics. *Eur J Cardio-thoracic Surg* 49:1578–1585. <https://doi.org/10.1093/ejcts/evz459>
46. Virues Delgadillo JO, Delorme S, El-Ayoubi R, DiRaddo R, Hatzikiriakos SG (2010) Effect of freezing on the passive mechanical properties of arterial samples. *J Biomed Sci Eng* 3:645–652. <https://doi.org/10.4236/jbise.2010.37088>
47. Gao F, Ohta O, Matsuzawa T (2008) Fluid-structure interaction in layered aortic arch aneurysm model: assessing the combined influence of arch aneurysm and wall stiffness. *Austral Phys Eng Sci Med* 31:32–41. <https://doi.org/10.1007/BF03178451>
48. Brown S, Wang J, Ho H, Tullis S (2013) Numeric simulation of fluid–structure interaction in the aortic arch. *Comput Biomech Med*. https://doi.org/10.1007/978-1-4614-6351-1_3
49. Raghavan ML, Vorp DA (2000) Toward a biomechanical tool to evaluate rupture potential of abdominal aortic aneurysm: identification of a finite strain constitutive model and evaluation of its applicability. *J Biomech* 33:475–482. [https://doi.org/10.1016/S0021-9290\(99\)00201-8](https://doi.org/10.1016/S0021-9290(99)00201-8)
50. Huh U, Lee CW, You JH, Song CH, Lee CS, Ryu DM (2019) Determination of the material parameters in the Holzapfel-Gasser-Ogden constitutive model for simulation of age-dependent material nonlinear behavior for aortic wall tissue under uniaxial tension. *Appl Sci* 9:1–18. <https://doi.org/10.3390/app9142851>
51. Azadani AN, Chitsaz S, Mannion A et al (2013) Biomechanical properties of human ascending thoracic aortic aneurysms. *Ann Thorac Surg* 96:50–58. <https://doi.org/10.1016/j.athoracsur.2013.03.094>
52. Olufsen MS, Peskin CS, Kim WY, Pedersen EM, Nadim A, Larsen J (2000) Numerical simulation and experimental validation of blood flow in arteries with structured-tree outflow conditions. *Ann Biomed Eng* 28:1281–1299
53. Boccadifuoco A, Mariotti A, Capellini K, Celi S, Salvetti MV (2018) Validation of numerical simulations of thoracic aorta hemodynamics: comparison with in vivo measurements and stochastic sensitivity analysis. *Cardiovasc Eng Technol* 9:688–706. <https://doi.org/10.1007/s13239-018-00387-x>
54. De Galarreta SR, Cazón A, Antón R, Finol EA (2017) The relationship between surface curvature and abdominal aortic aneurysm wall stress. *J Biomech Eng* 139:1–27. <https://doi.org/10.1115/1.4036826>
55. Rodríguez JF, Ruiz C, Doblaré M, Holzapfel GA (2008) Mechanical stresses in abdominal aortic aneurysms: influence of diameter, asymmetry, and material anisotropy. *J Biomech Eng* 130:021023. <https://doi.org/10.1115/1.2898830>
56. Rodríguez JF, Martufi G, Doblaré M, Finol EA (2009) The effect of material model formulation in the stress analysis of abdominal aortic aneurysms. *Ann Biomed Eng* 37:2218–2221. <https://doi.org/10.1007/s10439-009-9767-1>
57. Vande Geest JP, Schmidt DE, Sacks MS, Vorp DA (2008) The effects of anisotropy on the stress analyses of patient-specific abdominal aortic aneurysms. *Ann Biomed Eng* 36:921–932. <https://doi.org/10.1007/s10439-008-9490-3>
58. Condemi F, Campisi S, Viallon M, Troalen T, Xuexin G, Barker AJ, Markl M, Croisille P, Trabelsi O, Cavinato C, Duprey A (2017) Fluid-and biomechanical analysis of ascending thoracic aorta aneurysm with concomitant aortic insufficiency. *Ann Biomed Eng* 45:2921–2932. <https://doi.org/10.1007/s10439-017-1913-6>
59. Ong CW, Yap CH, Kabinejadian F et al (2018) Association of hemodynamic behavior in the thoracic aortic aneurysm to the intraluminal thrombus prediction: a two-way fluid structure coupling investigation. *Int J Appl Mech* 10:1–23. <https://doi.org/10.1142/S1758825118500357>
60. Natsume K, Shiiya N, Takehara Y, Sugiyama M, Satoh H, Yamashita K, Washiyama N (2017) Characterizing saccular aortic arch aneurysms from the geometry-flow dynamics relationship.

- J Thorac Cardiovasc Surg 153:1413-1420.e1. <https://doi.org/10.1016/j.jtcvs.2016.11.032>
61. Malek AM, Alper SL, Izumo S (2021) Hemodynamic shear stress and its role in atherosclerosis. *JAMA* 21:2035–2042. <https://doi.org/10.1001/jama.282.21.2035>
62. Khanafer KM, Bull JL, Berguer R (2009) Fluid-structure interaction of turbulent pulsatile flow within a flexible wall axisymmetric aortic aneurysm model. *Eur J Mech B/Fluids* 28:88–102. <https://doi.org/10.1016/j.euromechflu.2007.12.003>
63. Ong C, Kabinejadian F, Xiong F, Wong Y, Toma M, Nguyen Y, Chua K, Cui F, Ho P, Leo H (2019) Pulsatile flow investigation in development of thoracic aortic aneurysm: an in-vitro validated fluid structure interaction analysis. *J Appl Fluid Mech* 12:1855–1872. <https://doi.org/10.29252/jafm.12.06.29769>

Publisher's Note Springer Nature remains neutral with regard to jurisdictional claims in published maps and institutional affiliations.